IOP Publishing Measurement Science and Technology
Meas. Sci. Technol. 31 (2020) 045402 (11pp) https://doi.org/10.1088/1361-6501/ab5757

Artifactless, lens-free coherent microscopy with quasi-3D scanning

Cheng Guo[1,2], Xianming Liu[3], Xingchi Kan[4], Feilong Zhang[1,2], Jiubin Tan[1,2], Shutian Liu[5], Cuimei Tan[6] and Zhengjun Liu[1,2,7]

[1] Center of Ultra-Precision Optoelectronic Instrument Engineering, Harbin Institute of Technology, Harbin 150080, People's Republic of China
[2] Key Lab of Ultra-Precision Intelligent Instrumentation (Harbin Institute of Technology), Ministry of Industry and Information Technology, Harbin 150080, People's Republic of China
[3] School of Computer Science and Technology, Harbin Institute of Technology, Harbin 150080, People's Republic of China
[4] College of Veterinary Medicine, Jilin University, Changchun 130062, People's Republic of China
[5] Department of Physics, Harbin Institute of Technology, Harbin 150080, People's Republic of China
[6] Guangdong Provincial Key Laboratory of Modern Geometric and Mechanical Metrology Technology, Guangdong Institute of Metrology, Guangzhou 510405, People's Republic of China

E-mail: zjliu@hit.edu.cn

Received 16 September 2019, revised 8 November 2019
Accepted for publication 13 November 2019
Published 8 January 2020

Abstract

We propose a quasi-3D scheme to solve imaging artifacts from the laser source for lens-free holographic imaging. The scheme includes three steps: background noise removal, image alignment and twin-image elimination. The sample moves along the lateral direction and the imaging sensor is sequentially placed at different axial distances for data recording. With this volume data, the artifacts from the laser source can be effectively mitigated. The experiments show that a pixel-level imaging resolution (1.55 μm) over a field-of-view larger than 20 mm^2 can be achieved. The experiments with biological samples, including kidney and intestine pathological slides of rats, validate that this technique can realize dramatic image contrast and resolution enhancements compared to conventional lens-free holographic methods. Our work provides a new framework to suppress laser source artifacts for holographic imaging.

Keywords:image reconstruction techniques, phase retrieval, computational imaging

(Some figures may appear in colour only in the online journal)

1. Introduction

A lens-free holographic microscope [1] puts the imaging sensor chip close to the sample and runs a post-processing algorithm with raw holograms to output a micro-resolution image over a wide field-of-view (FOV). Without the precise control of the reference beam [2, 3], lens-free in-line holography has been developed in a powerful lab-on-a-chip device for imaging and measurement. Until now, it has been applied in point-of-care testing [4–7], refractive index measurement [8], air quality monitoring [9], particle tracking velocimetry [10] and pathological analysis [11].

[7] Author to whom any correspondence should be addressed.

However, holographic in-line configuration has the hazard of twin-image and laser source artifacts. The twin-image artifact originates from the superposition of the object's conjugate component. Laser source artifacts are composed of speckle noise and defocused crosstalk from the diffraction of dust on the collimated lens, which undermines the imaging resolution of lens-free holographic imaging. The extended ptychographic iterative engine (ePIE) algorithm [12–15] is an ideal strategy to mitigate these imaging artifacts, since it can achieve a joint reconstruction of the incident pattern and object. Nevertheless, the application of ePIE in lens-free imaging is limited by the huge data amount. For example, as done in [14, 15], if the overlapped ratio is greater than 90% and the probe size has hundreds of microns, the ePIE method

needs approximately 10 000 raw holograms to synthesize a FOV of 20 mm^2. Different from ePIE, multi-distance phase retrieval (MDPR) [16–19] only utilizes eight axial holograms to accomplish a whole-field lensless reconstruction. But laser source artifacts could lead to aligning problems and an unclear background for MDPR.

Inspired by these two methods, we propose a quasi-3D scanning strategy to mitigate these imaging artifacts. In the data acquisition, the sample scans in a lateral plane, and the imaging sensor is placed at different axial positions, thus a volume of data is recorded. In the data process, a weighted ePIE method is proposed to retrieve the incident pattern instead of the joint reconstruction of the object and incident pattern. Then, MDPR is introduced to eliminate the twin-image artifact. After this correction, the data amount of the raw holograms can be heavily decreased. Compared to the conventional ePIE method, our method accomplishes a data-efficient whole-field reconstruction, where only 100 raw holograms are required. In contrast with the conventional MDPR method, our method removes the aligning problem and background noise, enabling a dramatic enhancement of image contrast and resolution. Simulated results and experiments (resolution chart and pathology slides) have verified the improvement of the proposed technique.

2. Theory

The workflow of our quasi-3D scanning scheme is illustrated in figure 1. It includes three steps: background removal, image alignment and twin-image elimination. For data recording, a sample is laterally shifted with N_x by N_y and then the imaging sensor is axially moved N_z times. Thus a volume of intensity patterns ($N_x \times N_y \times N_z$) is obtained. In this configuration, the lateral dataset from the object shifts is used for background noise removal, which transforms the volume data into axial patterns. Then, the image alignment algorithm [20, 21] solves the aligning problem for the patterns. Finally, running MDPR with these aligned patterns outputs an artifact-free sample image.

Assuming that speckle noise and defocused crosstalk exist in the incident pattern, a direct approach to suppress these noises is to separate the object from the background image. Inspired by the ePIE method, we intuitively intend to shift a sample across the x–y plane to produce a sequence of diffraction patterns under a constant background illumination, and the background image can be extracted by ptychographic imaging. To simultaneously decrease the data amount and increase the FOV, we adopt full-field illumination rather than the conventional pinhole-shaped illumination. In this configuration, the ePIE with fewer raw holograms cannot be stably convergent. To address this issue, we propose a correction method, called weighted-projection ePIE (wePIE), to separate the object from the background noise.

If the object and background image are represented as O and P, the scattered wavefront radiated from the object is expressed as

$$\psi_i(x,y) = P(x,y)O_i(x-x_i, y-y_i), \tag{1}$$

for the ith lateral shift ($i = N_x \times N_y$). (x_i, y_i) is the magnitude of the lateral shift. The diffraction patterns on the imaging sensor are recorded as

$$I_i^n = \left|\mathrm{Ang}[\psi_i]_{Z_n}\right|^2, \tag{2}$$

where $\mathrm{Ang}[\cdot]_{Z_n}$ denotes the angular spectrum diffraction propagation operator over the distance Z_n. The index n ($n \in [1, N_z]$) corresponds to the number of axial movements of the imaging sensor. Diffraction distances Z_n are defined by the initial distance Z_0 and the equivalent interval d as $Z_n = Z_0 + (n-1)d$. At each Z_n, the background image can be extracted by running the wePIE algorithm with the lateral dataset. The operation details can be generalized as follows:

(a) Initializing the extended object and background image with matrices of ones; the product of these two components results in a transmissive function of the sample $\psi_i^k = P^k O_i^k$.

(b) The kth transmissive function related to the ith shift is propagated to a detecting plane and is given as

$$\Phi_i^k(x,y) = \mathrm{Ang}\left[\psi_i^k\right]_{Z_n}. \tag{3}$$

(c) The amplitude of the detecting plane is replaced with the square root of recorded intensity patterns. The synthesized pattern is inversely propagated to the sample plane $\bar{\psi}_i^k$ and is expressed as

$$\bar{\psi}_i^k(x,y) = \mathrm{Ang}\left[\sqrt{I_i^n}\frac{\Phi_i^k}{\left|\Phi_i^k\right|}\right]_{-Z_n}. \tag{4}$$

(d) Multiple guesses of the object and the background are calculated as

$$\bar{O}_i^k(x-x_i, y-y_i) = O_i^k(x-x_i, y-y_i) + \alpha\frac{\mathrm{conj}\left[P^k(x,y)\right]}{\left|P^k(x,y)\right|^2}\left[\bar{\psi}_i^k - \psi_i^k\right], \tag{5}$$

$$\bar{P}_i^k(x,y) = \beta\frac{\mathrm{conj}\left[O_i^k(x-x_i, y-y_i)\right]}{\left|O_i^k(x-x_i, y-y_i)\right|^2}\left[\bar{\psi}_i^k - \psi_i^k\right], \tag{6}$$

where the coefficients are the same as the typical ePIE method, i.e. $\alpha = \beta = 1$.

(e) As i scans from 1 to N_xN_y, the $(k+1)$th estimations of the object and background image are derived from

$$O^{k+1} = w\sum_{i=1}^{N_xN_y}\bar{O}_i^k \tag{7}$$

$$P^{k+1} = P^k + \frac{1}{N_xN_y}\sum_{i=1}^{N_xN_y}\bar{P}_i^k, \tag{8}$$

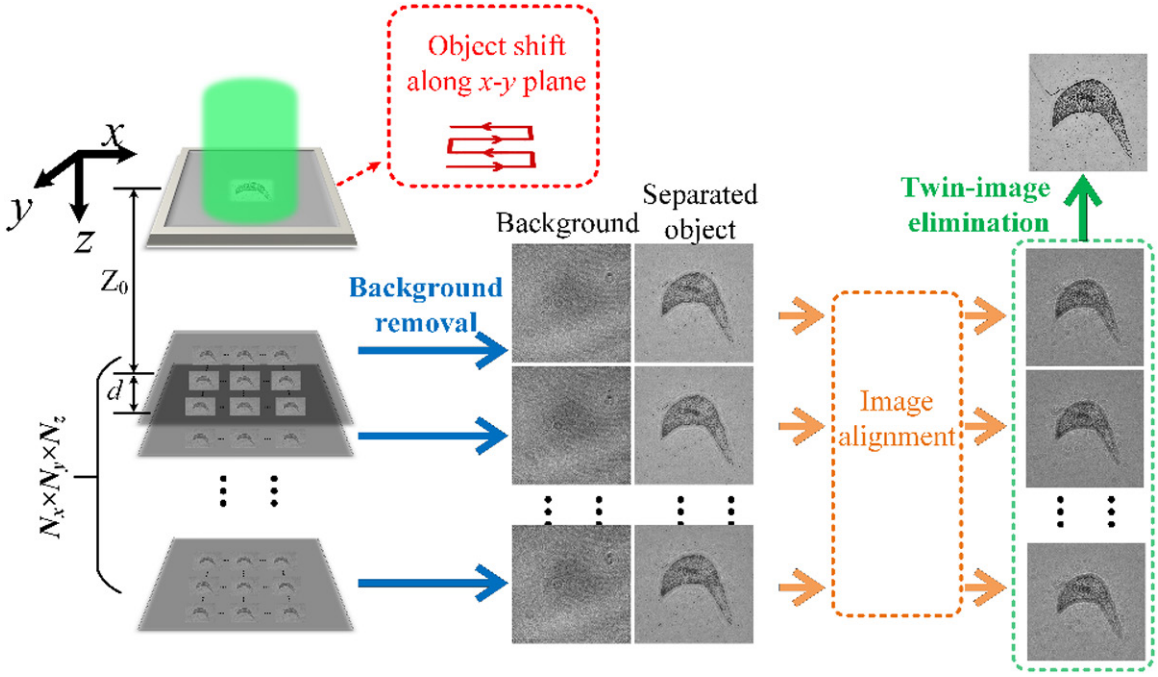

Figure 1. Workflow of our method.

where w represents the weighted coefficient matrix determined by the overlapped ratio.

(f) Repeating steps (b)–(e) achieves an intact separation for the object and background noise.

After the above operations, we can get an extended object with the wePIE method for every axial move when the sensor scans. The margin of the extended object is usually blurred and low-contrast, so the margin should be cropped and only the central shared part is kept. As lateral patterns at each axial distance are obtained with the wePIE method, a sequence of object estimations wrapped with a twin image are obtained, in which a volume of dataset ($N_x \times N_y \times N_z$) is converted into a 1D dataset ($1 \times N_z$) related to the axial distances.

The next step is to solve the aligning and pixelation problems for the axial dataset. As described in [21], tilt illumination causes an unaligned arrangement for object estimations. Thus a typical image alignment algorithm [20] is implemented on the object estimations to generate aligned patterns Ob_n. Then, Ob_n is propagated to the detecting plane with related distances Z_n and a group of axial diffraction patterns is obtained as follows

$$\Omega_n(x,y) = \left|\mathrm{Ang}[Ob_n]_{Z_n}\right|, \tag{9}$$

where the modulus of the diffraction patterns is retained and serves as the artifactless amplitude constraint for the MDPR. The imaging resolution of lens-free microscopy is limited by the pixelation problem. Detail larger than two pixels can be clearly retrieved according to the Nyquist–Shannon theorem. Here, a simple bicubic interpolation (upsampling factor = 2) is performed on these axial patterns. We will show that simply running MDPR with these upsampled data is effective in breaking the limit of the sampling theorem.

The MDPR algorithm with the upsampled modulus images is used to eliminate the twin image. The output of MDPR is indicated as S. The process of MDPR is described as follows: complex amplitude of sample S^0 is initialized with matrices of ones. At the kth iteration, S^k is forward-propagated to the detecting plane. After imposing the amplitude constraint and backward propagation, the $(k+1)$th sample is estimated as

$$S^{k+1} = \frac{1}{N_z}\sum_{n=1}^{N_z}\mathrm{Ang}\left[\Omega_n\frac{\mathrm{Ang}\left[S^k\right]_{Z_n}}{\left|\mathrm{Ang}[S^k]_{Z_n}\right|}\right]_{-Z_n}. \tag{10}$$

After some iterations, the twin image is completely eliminated and the complex amplitude of the sample is reconstructed with an imaging resolution of pixel level.

As a consequence, our quasi-3D scanning scheme is summarized as follows. The wePIE algorithm removes the noisy background and converts the volume data into the axial dataset. Then, the aligning and pixelation problems are solved by an image alignment algorithm and a bicubic interpolation. Finally, the processed axial dataset is fed to the MDPR algorithm to retrieve an artifactless sample image.

3. Simulation

3.1. Background noise removal

The simulation of separating an object from the background is given in figure 2. The ground truth images, including the object and background, are shown in figures 2(a) and (b). The product of figures 2(a) and (b) serves as a compound object function. This compound function with lateral shifts is propagated to the detecting plane and intensity patterns are generated. Here the ePIE and wePIE algorithms with intensity patterns are used to

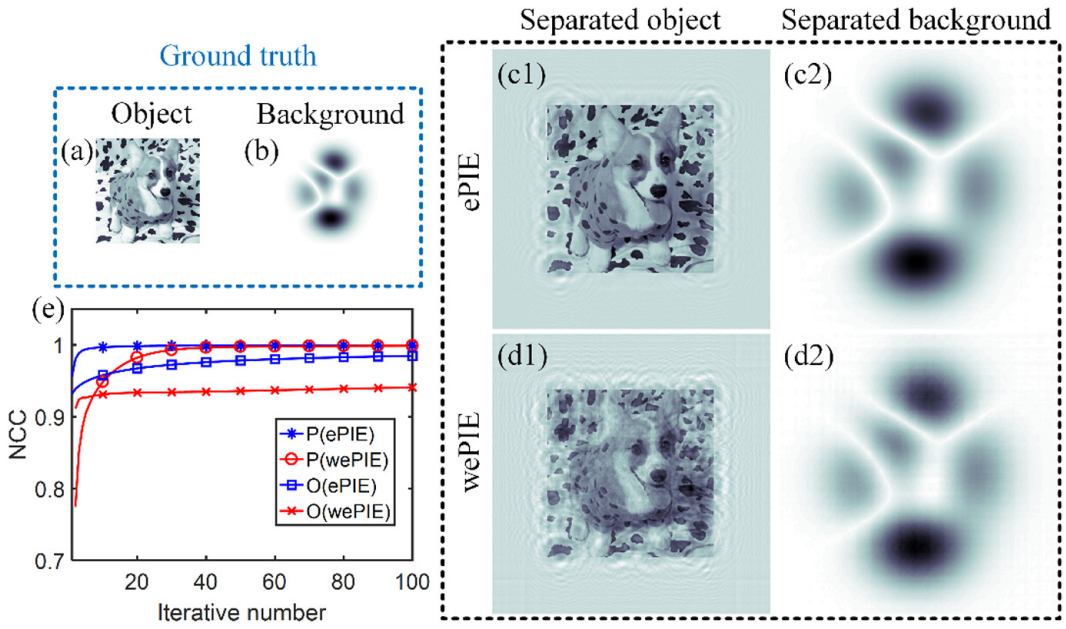

Figure 2. Numerical simulation of background removal for ePIE and wePIE. (a) Object; (b) background image; (c1) and (c2) retrieved object and background image of ePIE; (d1) and (d2) for wePIE; (e) convergence curve.

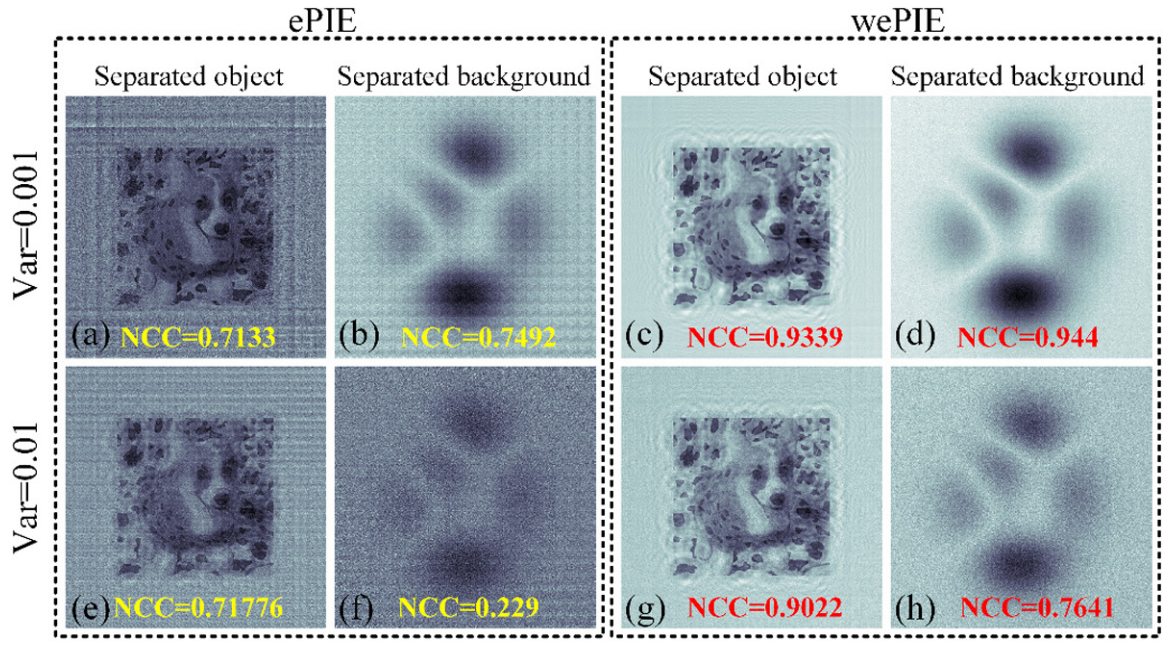

Figure 3. Numerical simulation of background removal with zero-mean Gaussian noise for the ePIE and wePIE. (a)–(d) Retrieved results for ePIE and wePIE with noise variance of 0.001; (e)–(h) results with noise variance of 0.01.

extract the background image. The simulated parameters are as follows: (a) the ground truth image is sampled with a size of 600 × 600 pixels; (b) the pixel size is 1.34 μm; (c) the diffraction distances are set as $Z_n = Z_0 + (n-1)d$ with $Z_0 = 1$ mm and $d = 1$ mm; (d) the wavelength of the plane wave is 532 nm; (e) the number of lateral shifts is 9×9 ($N_x = N_y = 9$) and the shift interval is 15 pixels. After 100 iterations, the object O and the background image P corresponding to Z_1 are simultaneously retrieved in figures 2(c1), (c2) and (d1), (d2) for ePIE and wePIE, respectively. Both methods completely separate the background image from the compound transmissive function. The retrieved object quality of ePIE is superior to that of wePIE. This difference can be quantitatively indicated by the normalized correlation coefficient (NCC), where this metric close to 1 denotes a better retrieved result. The NCC convergence curve of the two methods is plotted in figure 2(e). From the NCC curve, ePIE shows a faster convergence speed than wePIE for background removal in the noise-free case.

Simulations with the addition of Gaussian noise are displayed in figure 3. The parameters in figure 3 are the same as those in figure 2 except that a zero-mean Gaussian noise is imposed on the intensity patterns. After 100 iterations, the retrieved object and background with a noise variance of 0.001 are shown in figures 3(a)–(d) for ePIE and wePIE.

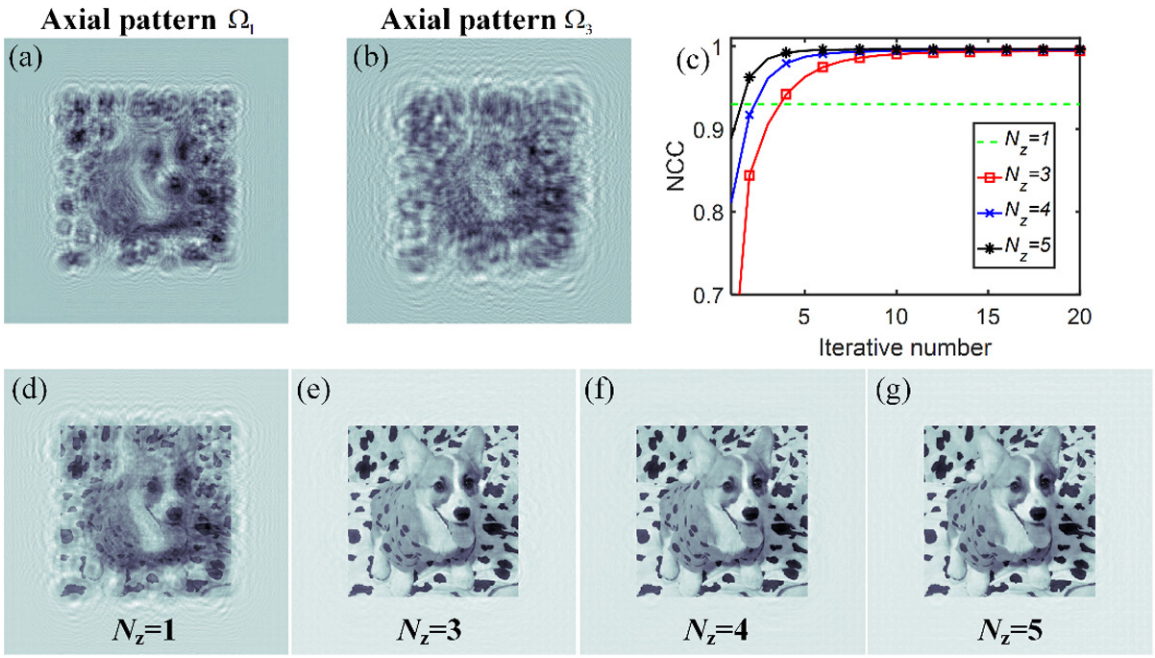

Figure 4. Numerical simulation of twin-image elimination with MDPR. (a) and (b) Axial modulus patterns in Z_1 and Z_3; (c) convergence curve; (d) retrieved amplitude by LIHM; (e)–(g) retrieved object by MDPR with 3, 4 and 5 axial modulus patterns.

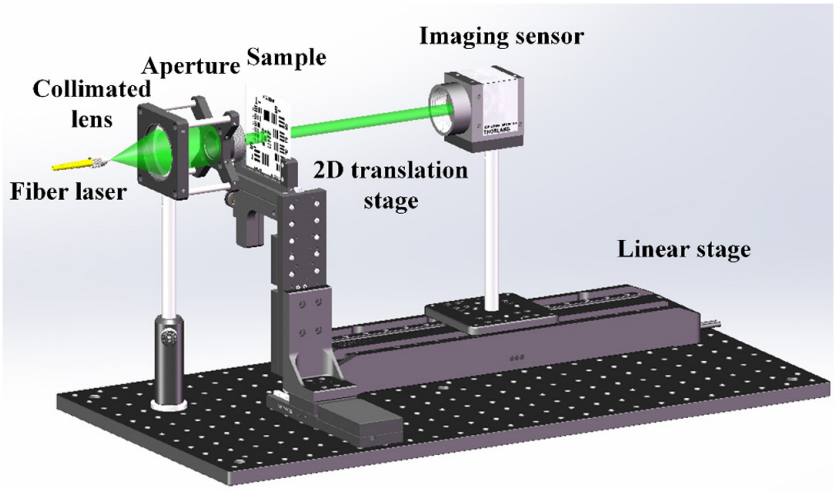

Figure 5. Experimental implementation of the lensless imaging with the quasi-3D scanning scheme.

Similarly, as noise variance is added to 0.01, the results of ePIE and wePIE are given in figures 3(e)–(h). Corresponding NCC values are labeled in each image. As clearly exhibited in figure 3, ePIE is very sensitive to noise. The NCC values dramatically decrease and the imaging quality is insufficient to separate the object from the background. On the contrary, wePIE possesses a compatible and robust imaging quality. Figures 2 and 3 prove that wePIE not only retrieves an intact background image but is also immune to noise.

3.2. Twin-image elimination

The retrieved object from wePIE still has the twin image, which will certainly reduce the imaging contrast. Here the multiple defocused images are used to remove the twin image. The number of axial measurements N_z is set as 5. After object estimations from Z_1 to Z_5 are separated by wePIE, these retrieved objects using equation (9) are converted into axial modulus patterns. The patterns in Z_1 and Z_3 are presented in figures 4(a) and (b). With the use of the pattern in figure 4(a), the amplitude image of the sample can be easily retrieved in figure 4(d) by lensless in-line holographic microscopy (LIHM [22]). It is seen that twin image obviously affects the imaging contrast for LIHM. Figures 4(e)–(g) are three retrieved amplitudes by MDPR with 3, 4 and 5 axial modulus patterns after 20 iterations. The twin image is clearly wiped out and imaging contrast is enhanced. The corresponding convergence curve is pictured in figure 4(c), which further validates the

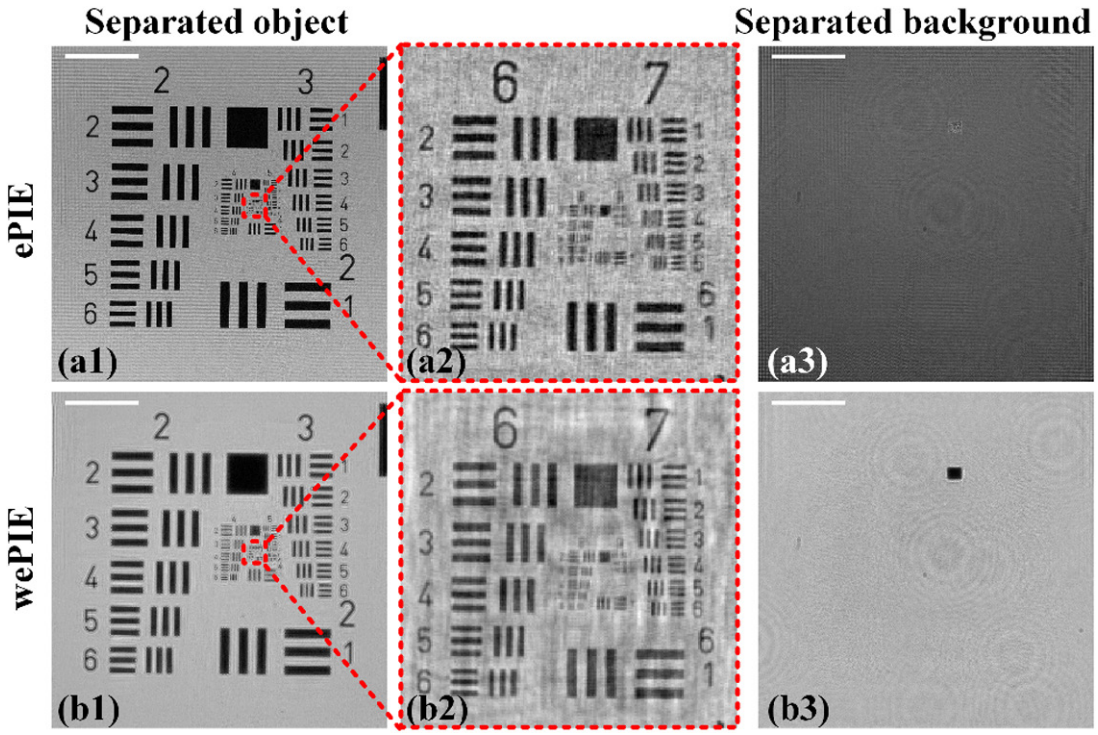

Figure 6. Experiment of background image removal for ePIE and wePIE. (a1) and (b1) Retrieved objects for ePIE and wePIE; (a2) and (b2) are the regions zoomed from (a1) and (b1); (a3) and (b3) are separated background images by ePIE and wePIE. The white bar corresponds to 1 mm.

effectiveness of MDPR. Ten iterations will be used in the following experiments, since iterative numbers larger than ten are stably convergent.

4. Experiment

The experimental implementation of our quasi-3D scanning scheme is shown in figure 5. A fiber laser (532 nm) equipped with a collimated lens (Thorlabs, $f = 200$ nm) outputs a plane wave to illuminate the sample. Two types of samples, resolution charts or pathology slides, are mounted on a lateral translation stage. This 2D stage is assembled from two 1D translation stages (Thorlabs, MTS50/M-Z8). The increment of the lateral shift is set as 50 μm in the experiment. A central region of 3400 × 3400 pixels in a CMOS sensor (Sony, IMX206, 1.34 μm × 1.34 μm) is selected for the on-chip measurement. This camera module is installed on a linear translation stage (M-403, Physik Instrumente Inc.) for the axial measurement and the interval of axial movement d is 2 mm.

The initial diffraction distance and the lateral shifts should be calibrated before performing our method. The calibration of the initial distance is regarded as a procedure of autofocusing. Refocusing images can be calculated by inversely propagating one of the diffraction patterns in Z_1 over different distances. The image sharpness of these refocusing images is assessed, and the peak value shows where the focusing plane is located. Here a gradient-based image sharpness metric in [23] is applied for this purpose. For the estimation of lateral shifts, a cross-correlation map is computed to track a lateral peak position between the central pattern and other patterns, which reduces the requirement of machine accuracy for the lateral translation stage.

Figure 6 is shown to compare the wePIE with the ePIE algorithm for the background noise removal. A standard positive USAF 1951 resolution chart (Edmund Optics) serves as the sample. The number of lateral shifts is 9 by 9. The initial axial distance between the sample and sensor is calibrated as 2.2 mm by the auto-focusing method. As the lateral intensity data in Z_1 are fed to two algorithms, the retrieved objects of ePIE and wePIE are cropped and shown in figures 6(a1) and (b1). The FOV is identified as 4.56 mm × 4.56 mm (approximately 21 mm^2). The central high-resolution regions of these retrieved targets are zoomed in figures 6(a2) and (b2). The background images are separated in figures 6(a3) and (b3). The imaging quality of wePIE is entirely superior to the ePIE result. Also, the result of ePIE presents a poor imaging contrast and element 6 of group 7 becomes distorted and blurred. As shown in figure 6(b3), a complete background image is extracted by wePIE. The defocused patterns from dust on the collimated lens and the glass slide are separated. Figure 6 verifies that wePIE is more robust and stable than ePIE for background noise removal.

Figure 7 shows the retrieved images of the resolution chart by LIHM, MDPR and our method. The retrieved amplitude of LIHM is exhibited in figure 7(a1). The corresponding details are zoomed in figures 7(a2)–(a4). LIHM could finish a high-resolution reconstruction, but its imaging contrast is constrained by the twin image. For MDPR, two groups of experiments are employed; one is to adopt the plane wave illumination, and the other removes the collimated lens and uses a fiber laser for spherical wave illumination. Twenty-one axial

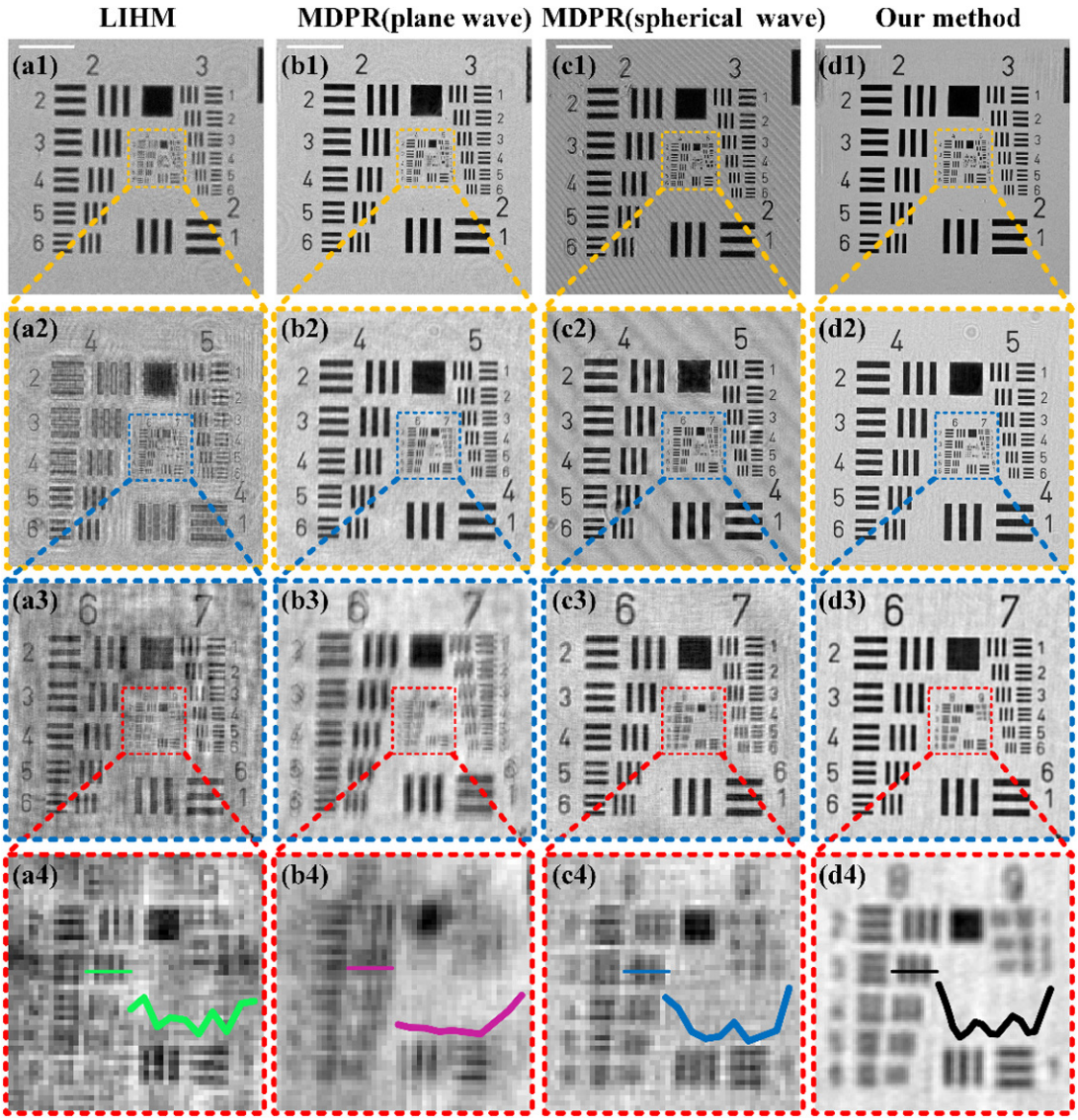

Figure 7. Experimental results of USAF 1951 positive resolution chart for different methods. (a1)–(a3) LIHM; (b1)–(b3) MDPR with plane wave illumination; (c1)–(c3) MDPR with spherical wave illumination; (d1)–(d3) our method. The white bar corresponds to 1 mm.

intensity patterns (interval $d = 1$ mm) are measured for the plane wave, and six axial patterns (interval $d = 0.1$ mm) are recorded for the spherical wave. The image alignment method in [20] is performed to align all axial patterns. With these aligned patterns inputted into MDPR, the retrieved results of the plane and spherical wave illumination are shown in figures 7(b1)–(b4) and (c1)–(c4), respectively. In figures 7(b1)–(b4), the image alignment algorithm is unable to solve the aligning problem caused by background noise, which makes the retrieved elements of group 7 blurred and unresolved. For the spherical illumination, this aligning problem could be alleviated in figure 7(c3) but the elements of group 8 cannot be clearly retrieved in figure 7(c4). Also, the interference-like fringe exists in the retrieved image shown in figure 7(c1).

Our method has the ability to thoroughly eliminate these artifacts of MDPR. During the procedure, wePIE (5×100 iterations), image alignment, bicubic interpolation and MDPR (ten iterations) are sequentially combined to process the recorded volume dataset. From the retrieved amplitudes in figures 7(d1)–(d4), our method achieves a dramatic enhancement for both imaging contrast and resolution. To show the comparison quantitatively, we draw the plotlines of element 3 of group 8 with different colors in figures 7(a4)–(d4). Particularly in figure 7(d4), element 3 of group 8 can be resolved by our method. This smallest resolved half-pitch reaches 1.55 μm and the pixel size of the sensor chip is 1.34 μm. It can be seen that the combination of images taken ultimately provides an image that has greater resolution than that of the image sensor used. To reach a higher resolution, multi-frame image super-resolution, including the gradient-based method [24] and shift-and-add algorithm [25, 26], can be embedded in the basic reconstruction process of our method.

It should be explained that the volume dataset ($9 \times 9 \times 5$) is entirely sufficient for artifact-free image reconstruction. We reduce the required axial and lateral measurement times to seek an optimal solution. As the number of axial patterns ranges from 2 to 5 and lateral movement is set as 3×3, 5×5, 7×7 and 9×9, the resolution charts are retrieved after 100

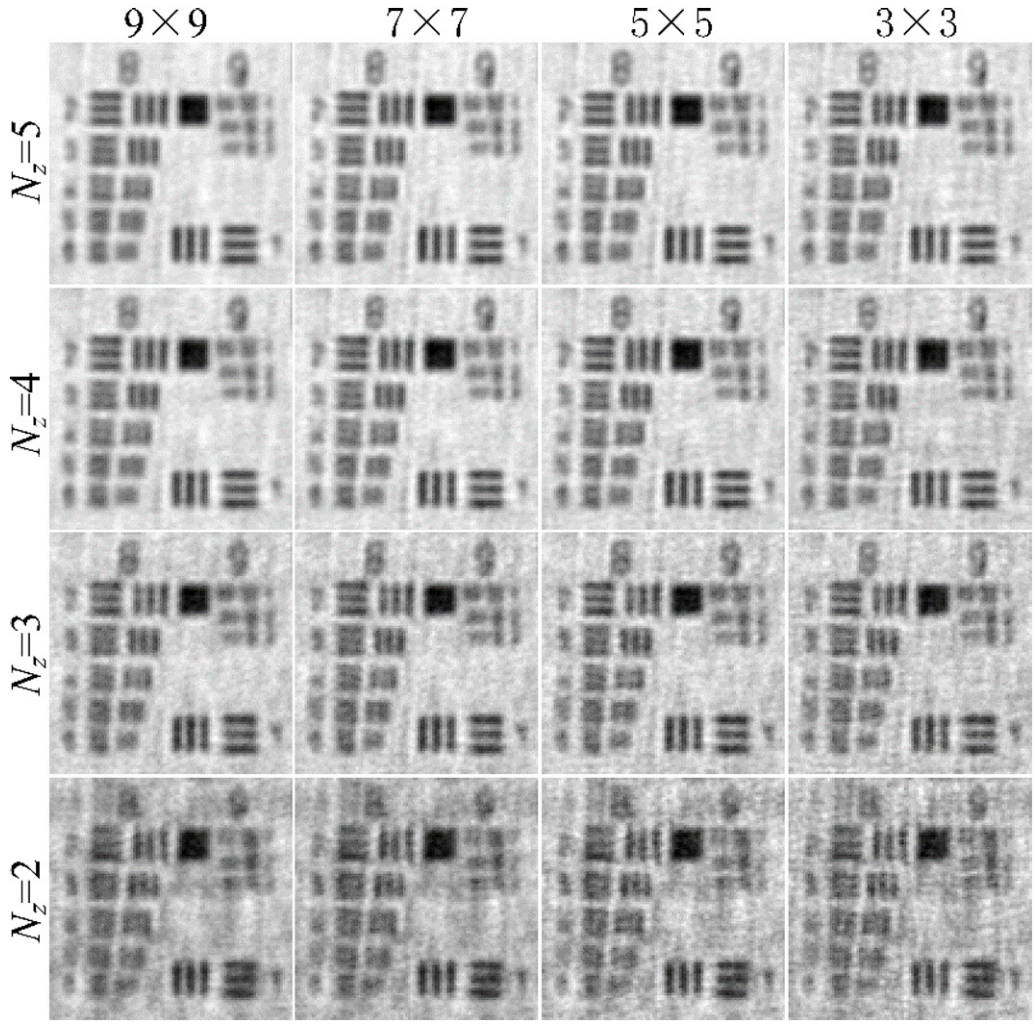

Figure 8. The retrieved resolution charts by different lateral and axial movement times.

Table 1. NCC values for different scanning strategies.

	9 × 9	7 × 7	5 × 5	3 × 3
$N_z = 5$	1	0.9987	0.9962	0.9875
$N_z = 4$	0.9950	0.9945	0.9923	0.9824
$N_z = 3$	0.9761	0.9754	0.9728	0.9605
$N_z = 2$	0.9363	0.9336	0.9286	0.9160

iterations. The corresponding higher resolution regions are given in figure 8. To quantitatively show this difference, the image with scanning times of 9 × 9 × 5 is chosen as a reference image. NCC values between the reference and retrieved images are listed in table 1. As shown in figure 8 and table 1, the NCC values lower than 0.99 undermine the imaging contrast, which proves that the minimum acceptable scanning strategy is 5 × 5 × 4 for reducing measurement loads. Therefore, we use the scanning number of 5 × 5 × 4 for the following experiments.

To show the data efficiency of our method, we provide the retrieved results of our method and ePIE in figure 9. As the scanning times of ePIE increase from 9 × 9 to 29 × 29, we can observe that the twin image and noisy background in figures 6(a1) and (a2) are eliminated in figures 9(a1)–(a3), where the synthesized FOV is 3.5 mm^2. In contrast, the results of our method using 5 × 5 × 4 are shown in figures 9(b1)–(b3), where the achieved FOV is approximately six-fold that obtained by the ePIE method. As shown in figure 9(a3) and (b3), element 6 of group 7 is still blurred with the ePIE method. This bad performance of ePIE is attributed to two aspects: firstly, the overlapped ratio is still too small to retrieve all the information; secondly, the lateral shifts are not accurate, and the shift estimation algorithm in [27] should be added in the ePIE method. Anyway, the further improvement of ePIE on the overlapped ratio and shift estimation actually makes it time-consuming and cumbersome for whole-field image reconstruction. Figure 9 proves that our method outperforms the ePIE method in terms of resolution and FOV.

We prepare two types of pathological slides, rat kidney and intestine, to test the capability of biomedical imaging. The kidney slide stained with hematoxylin and eosin (H&E) was purchased from Magnacol Ltd. The intestine slides were homemade by the College of Veterinary Medicine (Jilin University) [28]. The corresponding mice (C57BL/6) were purchased from the Center of Experimental Animals of Baiqiuen Medical College of Jilin University. The mice were anesthetized and their colons (approximately 2 cm)

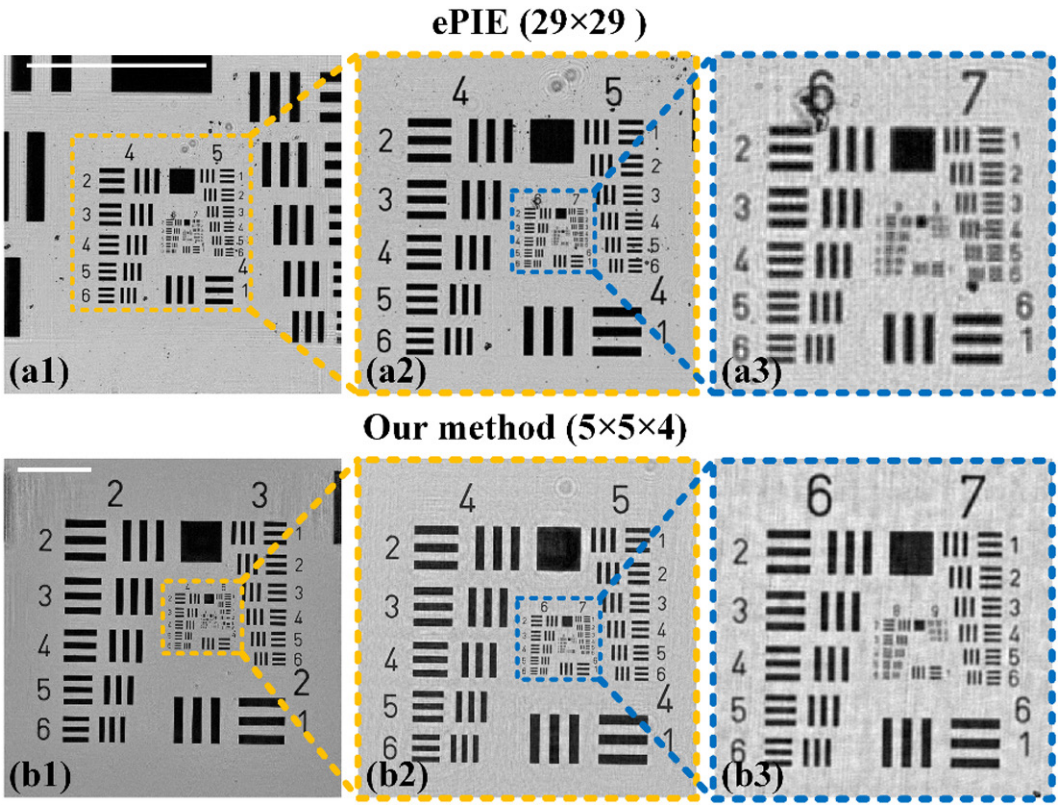

Figure 9. Comparison of ePIE with 29 × 29 raw holograms and our method with 100 raw holograms. (a1)–(a3) ePIE; (b1)–(b3) our method. The white bar corresponds to 1 mm.

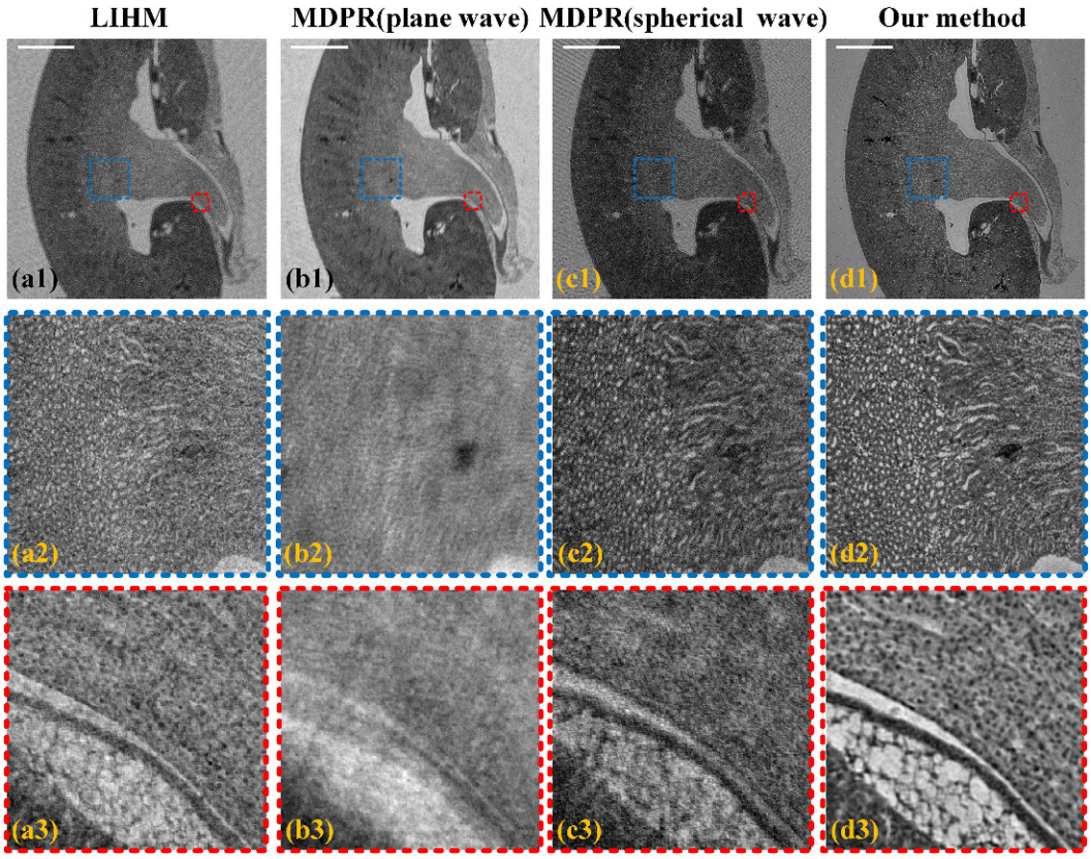

Figure 10. Experimental results of rat kidney for different methods. (a1)–(a3) LIHM; (b1)–(b3) MDPR with plane wave illumination; (c1)–(c3) MDPR with spherical wave illumination; (d1)–(d3) our method. The white bar corresponds to 1 mm.

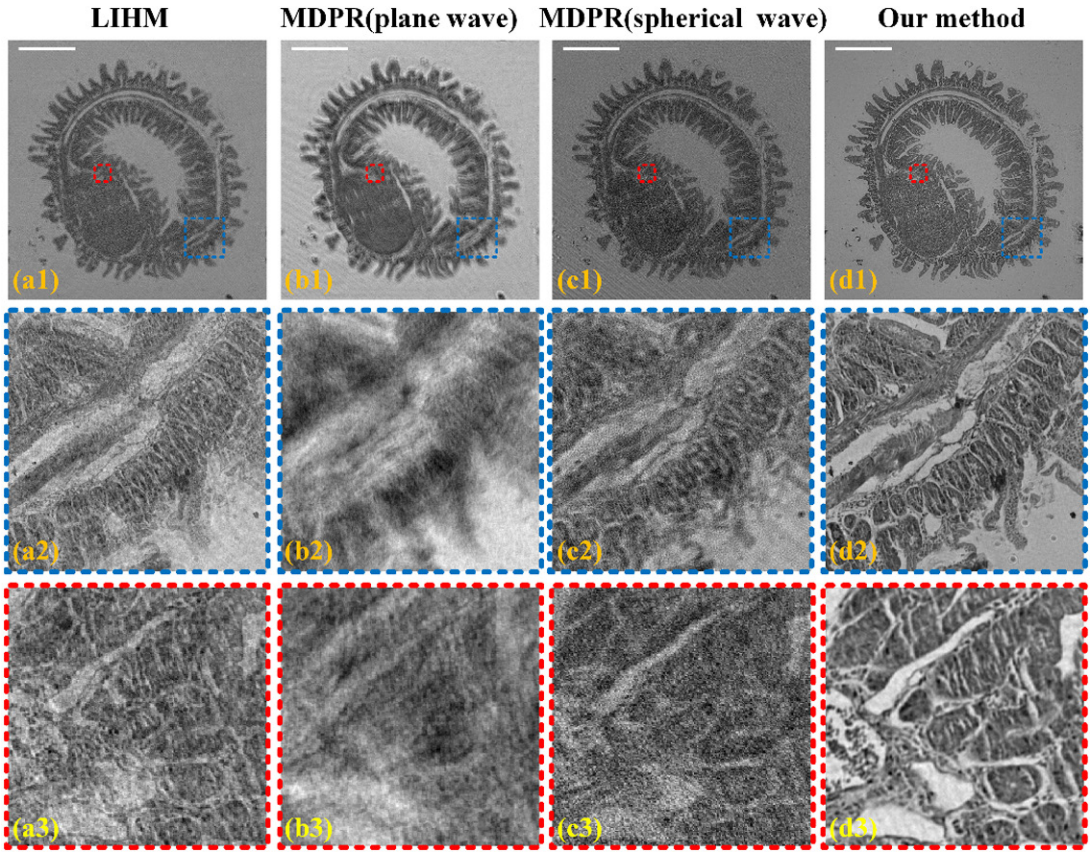

Figure 11. Experimental results of rat intestine for different methods. (a1)–(a3) LIHM; (b1)–(b3) MDPR with plane wave illumination; (c1)–(c3) MDPR with spherical wave illumination; (d1)–(d3) our method. The white bar corresponds to 1 mm.

were obtained and immersed in a phosphate buffer solution to remove the intestinal contents. Then the paraffin sections were prepared as follows: (a) fixed with formalin for 24 h; (b) graded dehydration with 70%, 85%, 95% and 100% ethanol was carried out for 15 min each time; (c) treated with 100% ethanol and xylene three times for 20 min each time; (d) paraffin was sequentially embedded, sectioned and stained with H&E. The initial sample-to-sensor distances of the kidney and intestine slides are calibrated as 3.9 mm and 2.12 mm by an auto-focusing algorithm. Different from the resolution chart, biological samples have a complex 3D structure. The thickness of pathology slides in our experiment was approximately 8 μm. The axial resolution of lens-free imaging is close to this sample thickness [29]. Hence, these three pathology slides are regarded as the thin sample for the image reconstruction.

The retrieved amplitudes of the kidney slide are shown in figures 10(a1)–(d1). The regions labeled with the blue and red boxes are displayed in figures 10(a2)–(d2) and (a3)–(d3). The sizes of the blue and red box are 670 μm × 670 μm and 268 μm × 268 μm. As the kidney slide is a dense sample, its imaging quality is easily impaired by background noise. The results of figures 10(a3)–(c3) reveal this drawback for LIHM and MDPR. The region of the red box is only reconstructed by our scheme. In particular, the cell nucleus of the pelvis area in figure 10(d3) can be resolved and observed. To further test the stability of our method, the intestine slide made by ourselves is used as the sample and its retrieved amplitudes are shown in figure 11. The two labeled regions are enlarged in figures 11(a2)–(d2) and (a3)–(d3). Similar to figure 10, our method has the apparent advantage in the image reconstruction of the rat intestine, where artifact noise caused by laser illumination is effectively eliminated.

5. Conclusion

We propose a quasi-3D scanning scheme to mitigate imaging artifacts for a lens-free microscope with laser illumination. A volume of intensity data is measured by lateral object shifts and axial sensor movement. Our method is composed of background noise removal, image alignment and twin-image elimination: the wePIE algorithm is used to separate background noise for each layer of lateral patterns and converts volume data into an axial dataset; then, the image alignment and the bicubic interpolation are performed to form an artifact-less axial modulus dataset; finally, a complex-valued sample image is retrieved by MDPR with the processed axial patterns. Experiments show that the imaging artifacts can be effectively eliminated and a pixel-level imaging resolution over a FOV larger than 20 mm^2 can be achieved. For the imaging of pathology slides, the kidney and intestine of rats are reconstructed with enhanced image contrast and resolution.

This work gives a stable and robust imaging prototype for the laser-based lens-free microscope. We also provide some further applications of our method. Firstly, equipped with a color image fusion technique, our method could enable a color

artifact-free point-of-care for pathological slide imaging. Secondly, as the linear stage is replaced with an LED matrix, the phase imaging capacity of our method could facilitate a portable and miniaturized device to monitor waterborne parasitic infections.

Acknowledgments

This work is supported by the National Natural Science Foundation of China (61575055, 61575053, 11874132 and 61975044), and the Open Fund Project Foundation of Guangdong Provincial Key Laboratory of Modern Geometric and Mechanical Metrology Technology (SCMKF201804). The authors are indebted to two reviewers for helpful comments and suggestions.

ORCID iDs

Shutian Liu https://orcid.org/0000-0001-9748-0175
Zhengjun Liu https://orcid.org/0000-0003-2886-8496

References

[1] Greenbaum A, Luo W, Su T, Göröcs Z, Xue L, Isikman S O, Coskun A F, Mudanyali O and Ozcan A 2012 Imaging without lenses: achievements and remaining challenges of wide-field on-chip microscopy *Nat. Methods* **9** 889–95
[2] Zhang X, Wang J, Zhang X, Xu M, Zhang H and Jiang X 2018 Correction of phase-shifting error in wavelength scanning digital holographic microscopy *Meas. Sci. Technol.* **29** 055002
[3] Dong J, Jia S and Jiang C 2018 Correlation-coefficient based auto-focusing algorithm for focus detection in shape measurement using two-source digital holographic interferometry *Meas. Sci. Technol.* **29** 085012
[4] Tseng D, Mudanyali O, Oztoprak C, Isikman S O, Sencan I, Yaglidere O and Ozcan A 2010 Lensfree microscopy on a cellphone *Lab Chip* **10** 1787–92
[5] Bishara W, Sikora U, Mudanyali O, Su T, Yaglidere O, Luckhartb S and Ozcan A 2011 Holographic pixel super-resolution in portable lensless on-chip microscopy using a fiber-optic array *Lab. Chip* **11** 1276–9
[6] Jang A, Zou Z, Lee K K, Ahn C H and Bishop P L 2011 State-of-the-art lab chip sensors for environmental water monitoring *Meas. Sci. Technol.* **22** 032001
[7] Berner M, Hilbig U, Schubert M B and Gauglitz G 2017 Laser-induced fluorescence detection platform for point-of-care testing *Meas. Sci. Technol.* **28** 085701
[8] Bian Y, Zhang Y, Yin P, Li H and Ozcan A 2018 Optical refractometry using lensless holography and autofocusing *Opt. Express* **26** 29614–28
[9] Wu Y *et al* 2017 Air quality monitoring using mobile microscopy and machine learning *Light Sci. Appl.* **6** e17046
[10] Satake S, Unno N, Nakata S and Taniguchi J 2016 3D measurement of the position of gold particles via evanescent digital holographic particle tracking velocimetry *Meas. Sci. Technol.* **27** 084009
[11] Greenbaum A, Zhang Y, Feizi A, Chung P, Luo W, Kandukuri S R and Ozcan A 2014 Wide-field computational imaging of pathology slides using lensfree on-chip microscopy *Sci. Trans. Med.* **6** 267ra175
[12] Maiden A M and Rodenburg J M 2009 An improved ptychographical phase retrieval algorithm for diffractive imaging *Ultramicroscopy* **109** 1256–62
[13] Rodenburg J M and Faulkner H M L 2004 A phase retrieval algorithm for shifting illumination *Appl. Phys. Lett.* **85** 4795–7
[14] Claus D and Rodenburg J M 2015 Pixel size adjustment in coherent diffractive imaging within the Rayleigh–Sommerfeld regime *Appl. Opt.* **54** 1936–44
[15] Claus D and Rodenburg J M 2019 Diffraction-limited superresolution ptychography in the Rayleigh-Sommerfeld regime *J. Opt. Soc. Am.* A **36** A12–9
[16] Pedrini G, Osten W and Zhang Y 2005 Wave-front reconstruction from a sequence of interferograms recorded at different planes *Opt. Lett.* **30** 833–5
[17] Greenbaum A and Ozcan A 2012 Maskless imaging of dense samples using pixel super-resolution based multi-height lensfree on-chip microscopy *Opt. Express* **20** 3129–43
[18] Guo C, Shen C, Li Q, Tan J, Liu S, Kan X and Liu Z 2018 A fast-converging iterative method based on weighted feedback for multi-distance phase retrieval *Sci. Rep.* **8** 6436
[19] Greenbaum A, Sikora U and Ozcan A 2012 Field-portable wide-field microscopy of dense samples using multi-height pixel super-resolution based lensfree imaging *Lab Chip* **12** 1242–5
[20] Guizar-Sicairos M, Thurman S T and Fienup J R 2008 Efficient subpixel image alignment algorithms *Opt. Lett.* **33** 156–8
[21] Guo C, Li Q, Tan J, Liu S and Liu Z 2018 A method of solving tilt illumination for multiple distance phase retrieval *Opt. Lasers. Eng.* **106** 17–23
[22] Feng S and Wu J 2017 Resolution enhancement method for lensless in-line holographic microscope with spatially-extended light source *Opt. Express* **25** 24735–44
[23] Guo C, Zhao Y, Tan J, Liu S and Liu Z 2018 Adaptive lensfree computational coherent imaging using autofocusing quantification with speckle illumination *Opt. Express* **26** 14407–20
[24] Luo W, Zhang Y, Feizi A, Gorocs Z and Ozcan A 2016 Pixel super-resolution using wavelength scanning *Light. Sci. Appl.* **5** e16060
[25] Navruz I, Coskun A F, Wong J, Mohammad S, Tseng D, Nagi R, Phillips S and Ozcan A 2013 Smart-phone based computational microscopy using multi-frame contact imaging on a fiber-optic array *Lab Chip* **13** 4015–23
[26] Farsiu S, Robinson M D, Elad M and Milanfar P 2004 Fast and robust multiframe super resolution *IEEE Trans. Image Process.* **13** 1327–44
[27] Zhang F, Peterson I, Comamala J V, Diaz A, Berenguer F, Bean R, Chen B, Menzel A, Robinson I K and Rodenburg J M 2013 Translation position determination in ptychographic coherent diffraction imaging *Opt. Express* **21** 13592–606
[28] Chen G, Ran X, Li B, Li Y, He D, Huang B and Wang W 2018 Sodium butyrate inhibits inflammation and maintains epithelium barrier integrity in a TNBS-induced inflammatory bowel disease mice model *EBioMedicine* **30** 317–25
[29] Isikman S O, Bishara W, Sikora U, Yaglidere O, Yeah J and Ozcan A 2011 Field-portable lensfree tomographic microscope *Lab Chip* **11** 2222–30